Materials and Design 90 (2016) 815–819

Contents lists available at ScienceDirect

Materials and Design

journal homepage: www.elsevier.com/locate/jmad

High-temperature post-processing treatment of silica nanofoams of controlled pore sizes and porosities

Cang Zhao [a], Meng Wang [a], Yang Shi [b], Jianguo Cao [c], Yu Qiao [a,b,*]

[a] Department of Structural Engineering, University of California — San Diego, La Jolla, CA 92093-0085, USA
[b] Program of Materials Science and Engineering, University of California — San Diego, La Jolla, CA 92093, USA
[c] School of Mechanical Engineering, University of Science and Technology of Beijing, Beijing 100083, China

ARTICLE INFO

Article history:
Received 7 January 2015
Received in revised form 28 October 2015
Accepted 31 October 2015
Available online 1 November 2015

Keywords:
Pore size
Porosity
Amorphous
Silica
Monolith
Nanoporous

ABSTRACT

The pore size and the porosity of a nanoporous silica are often highly correlated. In the current investigation, based on the phenomenon that calcination temperature has a much more pronounced influence on the porosity than the pore size, we developed the post-processing calcination (PPC) technique to decouple the pore size and the porosity. As PPC temperatures were precisely controlled for silica monoliths of different initial pore sizes, their porosities could be tailored to a similar level, while the changes in pore sizes were quite mild. Powder X-ray diffraction analysis showed that the PPC treatment did not affect the amorphous nature of the silica phase.

1. Introduction

Nanoporous materials are being intensively studied in chemical, environmental, biological, energy, and medical science and engineering areas [1–6], and recently also in mechanical engineering [7–10]. A nanoporous material may be in powder form, in membrane form, or in monolithic form. Particularly, nanoporous monoliths, which will be referred to as nanofoams in the following discussion, are important to applications where a certain structural integrity is required for filtration, absorption and adsorption, purification, or gas/liquid conduction components [11–13]. A nanofoam has a macroscopic size, while the nanopores provide a large inner surface area and a confining nanoenvironment [14,15].

Nanofoams with the average pore sizes spanning from a few nm to hundreds of nm can be made of metals/alloys, polymers, or ceramics [11–13]. Metallic nanofoams may be synthesized by platinum, gold, copper, etc. through dealloying, templating, nanosmelting, combustion synthesis, etc. [12,16–18]. Polymeric nanofoams can be prepared via co-polymering, gas dissolution foaming, extrusion, etc. [11,19–21]. Ceramic nanofoams include nanoporous silica (SiO_2), alumina (Al_2O_3), etc. They can be processed through sol–gel method [13,22–24]. The processing techniques of silica nanofoams have been well developed for several decades [25]. Their average pore sizes could be reduced to a few nm [26], and their porosities could be more than 90% [27]. In this article, the term "pore size" refers to the average pore size, unless it is redefined.

For many applications, the porosity, c, and the pore size, d, of nanofoams need to be independently adjusted in desired ranges. For instance, while the specific surface area increases monotonously with the porosity, if the ligament length is too small the strength of a nanofoam would be low, so that the structural robustness is lost [27]. For another example, reducing the pore size would lead to a larger total surface area; yet for conduction of solvated molecules or ions the pore size must be sufficiently large, even if the pore surfaces are nominally wettable [28,29].

The porosity and the pore size of a nanofoam are often coupled [22,30,31]. For instance, in a sol–gel process, a powerful approach to vary the pore size is to change the mass ratio of different components [22,24,32]. For another example, the silica nanofoams synthesized via Shoup's method [22] have a wide range of pore sizes: The silica with the pore size of ~310 nm has a porosity of ~76% (density ~0.52 g/cm^3), while the silica with the pore size of ~50 nm has a porosity of ~86% (density ~0.32 g/cm^3).

In the current study, based on the phenomenon that the pore size and the porosity have different sensitivities to the calcination temperature, we developed a post-processing calcination (PPC) technique for silica nanofoams, to produce samples of similar porosity but different pore sizes. This research has a wide applicability for catalysis, absorption

* Corresponding author.
E-mail address: yqiao@ucsd.edu (Y. Qiao).

http://dx.doi.org/10.1016/j.matdes.2015.10.164
0264-1275/

and adsorption, energy conversion, and energy absorption, to name a few.

2. Experimental

Silica nanofoams with various average pore sizes were first synthesized, following the works of [22] for the foams with the average pore sizes smaller than 500 nm and [13,33] for the foams with the average pore sizes larger than 1 μm, respectively. In the former method [22], Sigma-Aldrich Ludox HS-40 colloidal silica was mixed with PQ Kasil-1 potassium silicate solution in a flask under magnetic stirring for 30 min, with the mass ratio in the range from 1:99 to 40:60. A larger colloidal silica amount tended to cause a reduced pore size. A 25 wt.% formamide solution, which was diluted in water with the mass ratio of 40:60, was slowly added to the silica–silicate mixture and vigorously mixed by a magnetic stirrer for 30 min. Then, the solution was transported into a polypropylene plastic vial with the inner diameter of 35.6 mm and the height of 16.3 mm. After aging at room temperature for 24 h, the wet gels were rinsed first by 1 M ammonium nitrate, then by 1 M nitric acid, then by deionized water at about 90 °C, and finally by pure methanol at room temperature. In the latter method [13,33], Sigma-Aldrich tetramethyl orthosilicate (TMOS, 98%) was added to a 0.01 M aqueous solution of acetic acid, and was thoroughly mixed in a flask under magnetic stirring for 30 min. In the acetic acid solution, Sigma-Aldrich polyethylene glycol (PEG, with the average molecular weight of 10,000) had been dissolved. The TMOS to PEG mass ratio varied from 3.0 to 7.2, so as to tailor the pore size. The mixture was then transported into a polypropylene plastic vial with the inner diameter of 46.2 mm and the height of 21.6 mm. After aging at 40 °C for 72 h, the gels were washed sequentially by 0.1 M aqueous ammonia solution at about 120 °C, then by 0.1 M nitric acid and deionized water at about 90 °C, and finally by pure methanol at room temperature. In both methods, each step of the rinsing process was repeated more than five times. After that, the silica monoliths were thermally treated in a VWR 1330GM oven at 80 °C for 72 h.

The obtained silica monoliths had different average pore sizes and porosities, and the pore size and the porosity were strongly correlated, as shown in Fig. 1(a). The average pore size was measured by mercury porosimetry (Table 1), and the porosity was calculated from the mass density. In order to decouple these two important parameters, a post-processing calcination (PPC) treatment was carried out on the silica monoliths in a MTI GSL-1700X horizontal tube furnace at selected temperatures (T_s) for 1 h. The PPC temperatures ranged from 850 °C to 1265 °C; it would affect both of the porosity and the pore size, but at different rates, as will be discussed in the next section. The ramp rate was initially set as 3 °C/min to keep the total heating time relatively short; and when the temperature was less than 100 °C away from T_s, was reduced to 1 °C/min, to minimize over-shooting.

To obtain homogeneous samples, the surface layers [34,35] of PPC-treated silica nanofoams were removed by a set of silicon carbide sandpapers. Before the PPC treatment, the thickness of the monolithic silica samples was 10–14 mm. After the PPC treatment, the thickness shrank to about 8–9 mm. Nearly 1.5 mm thick surface layers from the top and the bottom of the samples were first removed by 320-grit sandpapers, followed by further polishing with 600-grit sandpapers until the sample thickness was around 5 mm. Then, the sample thickness was reduced to about 4.75 mm by 1200-grit sandpapers and finally to about 4.50 mm by 2500-grit sandpapers.

The porosities of the silica nanofoams were calculated from their mass densities [36]: $c = 1 - \rho / \rho_n$, where ρ is the sample density and $\rho_n = 2.2$ g/cm^3 is the density of solid amorphous silica [25]. The total specific pore volume was estimated using $\nu = c \cdot V_t / m$ [36], where V_t is the sample volume and m is the sample mass. The dimensions and the porosities are shown in Table 2 and Fig. 2.

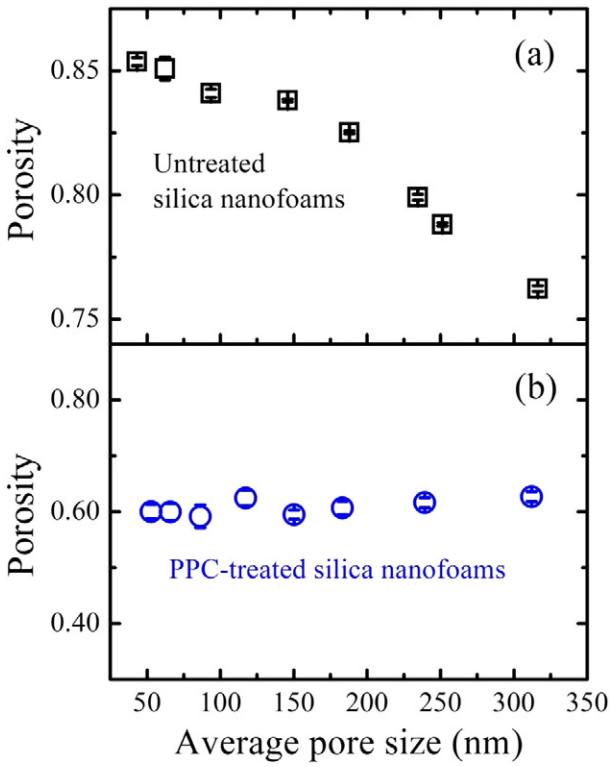

Fig. 1. The relationship between the pore size and the porosity of (a) untreated and (b) PPC-treated silica nanofoams.

The pore size was characterized by the well-established Washburn equation [37,38]: $d = 4\sigma \cdot \cos\theta / P_{Hg}$, where P_{Hg} is the infiltration pressure, $\sigma = 0.484$ N/m is the surface tension of mercury, and θ–140° is the contact angle. The mercury porosimetry was conducted by immersing 0.5–1.5 g silica nanofoam in mercury in a hardened steel cylinder with a closed bottom end. The inner diameter of the cylinder was 19.05 mm, and the height was about 40 mm. The top of the cylinder was sealed by a hardened steel piston, equipped with a reinforced polyurethane o-ring. In an Instron 5582 machine, the piston was intruded into the cylinder at a constant rate of 0.10 mm/min. The piston force was measured by an Instron 50KN loadcell; the piston displacement was recorded continuously by an Instron linear voltage displacement transducer (LVDT). The system volume change, V, was calculated as the piston displacement multiplied by the piston cross-sectional area; the piston pressure, P, was calculated as the piston force divided by the piston cross-sectional area. Fig. 3 shows typical infiltration curves. The profile of the infiltration plateau, P_{Hg}, indicates the distribution of pore size. The width of the infiltration plateau is associated with the pore volume. Fig. 4 shows a typical curve of the first derivative of P with respect to V, dP/dV. It was used to determine the range of the infiltration plateau. For self-comparison purposes, the beginning point was taken as the location where dP/dV abruptly dropped; the ending point was determined by the reference curve, 0.168 cm^3 away from the peak loading (dP/dV started to depart from zero). From the infiltration plateau, according to the Washburn Equation, the minimum and the maximum pore size were calculated, and the range of the pore size is listed in Table 1. The average pore size was set as the average value of the minimum and the maximum values, and the results are listed in Table 2. To evaluate the subcategory of nanopores, the specific pore volume of macropores was calculated through $\nu' = V/m$, where V is the pore volume determined from the width of the infiltration plateau. The ratio of ν'/ν was used to estimate the volume percentage of macropores. The mercury porosimetry results and the key processing parameters are summarized

Table 1
Results of mercury porosimetry.

Component mass ratio	TMOS to PEG	Colloidal silica to potassium silicate							
	5.5:1.0	1.3:98.7	7.5:92.5	12.5:87.5	17.0:83.0	22.5:77.5	27.5:72.5	35:65	40:60
PPC temperature (°C)	1230	1260	1262	1260	1258	1254	1251	1239	1228
Mercury infiltration pressure range (MPa)	[0.75–1.89]	[3.85–6.21]	[5.06–8.01]	[6.71–10.20]	[8.45–11.87]	[10.96–14.93]	[14.77–20.55]	[19.37–26.80]	[24.45–32.91]
Pore size range (nm)	[780–1980]	[240–390]	[190–290]	[150–220]	[130–180]	[100–140]	[70–100]	[60–80]	[40–60]
Specific volume of macropores (cm^3/g)	0.61	0.61	0.61	0.58	0.57	0.59	0.60	0.58	0.56

in Table 1. Fig. 1(b) shows the porosity of PPC-treated silica foams as a function of the pore size.

The PPC-treated silica nanofoams were analyzed through powder X-ray diffraction, by using a Bruker D8 Advance Diffractometer at 40 kV and 40 mA for Cu Kα ($\lambda = 1.5418$ Å). The scan speed was 0.1 s/step; the step size was 0.02°; the 2θ range was 10° to 80°. The XRD results are shown in Fig. 5. The silica nanofoams were also observed under a FEI-XL30 environmental scanning electron microscope (SEM) at 20 kV, with a spot size of 3.0. The SEM samples had been coated with iridium using an Emitech K575X sputter coater at 85 mA for 6 s prior to the observation. Fig. 6 shows typical SEM images.

3. Results and discussion

Fig. 1(a) indicates that, without any PPC treatment, the nanoporous silica samples demonstrate a strong correlation between the porosity and the pore size. With the increase in the colloidal silica content, on the one hand, finer structures would be formed during phase separation, leading to a smaller average pore size [22]; on the other hand, the weight fraction of potassium silicate, which would be dealkalized and polymerized [22], is also reduced, so that the porosity becomes higher. Such a phenomenon is quite common in nanoporous materials processing [e.g. 22,24,32].

After a silica monolith is synthesized, if it is calcined at a high temperature, the porous structure could be largely modified. As shown in Fig. 2 (a), when the PPC temperature, T_s, varies from 850 °C to 1265 °C, the porosity (c) can be adjusted in a wide range highly nonlinearly: From 850 °C to about 1100 °C, the porosity keeps nearly constant, ~76–85%; from 1100 °C to 1265 °C, the porosity decreases rapidly. For amorphous silica, it is the energy, E_f, obtained by the reduction in surface area that promotes the viscous flow and the elimination of pores; the obtained energy is the product of the specific surface energy (γ) and the variation in surface area (A) [25]. According to Frenkel's cylinder model [39], the calcination rate is proportional to $\gamma/(\eta \cdot d)$, where η is the viscosity and d is the pore size. When the calcination temperature is at the vicinity of the glass transition point, T_g, of amorphous silica ~1200 °C [40], the viscosity of silica is highly dependent on temperature, resulting in a rapid change in porosity [25]. This effect is more pronounced as the initial colloidal silica to potassium silicate ratio is higher, since smaller pores have a larger specific surface area; that is, to reach a similar porosity, within the same treatment time, lower calcination temperature is needed for smaller pores. According to Fig. 2(b), the PPC temperature effect on the average pore size (d) is quite mild. As T_s rises from 850 °C to about 1265 °C, the average pore size changes somewhat linearly by 10–20%, within the range of pore size distribution, suggesting that during the PPC process larger pores tend to shrink more slowly [25,39]. The relatively mild variation in average pore size should be attributed to the balance between the configuration change in smaller pores and the reduction of larger pores [25,41].

The difference in the T_s-c and T_s-d relationships provides a feasible method to independently adjust the pore size and the porosity. As we begin with silica monoliths of desired pore sizes but different porosities, and as the PPC treatment is conducted at appropriate temperatures, the pore sizes would change only slightly while the porosity can be greatly adjusted. Fig. 1(b) demonstrates that the PPC technique is quite successful. Following the optimized processing parameters listed in Table 1, the porosity of the treated silica nanofoams is similar, around 60%, while the pore size is controlled from tens of nm to more than 1 μm. Table 2 shows that all the PPC-treated samples have a similar density of about 0.85 g/cm^3, corresponding to a total specific pore volume of ~0.7 cm^3/g.

The pore size distributions in the above discussion are measured through the classic Washburn method, since the larger pore sizes exceed the range of gas absorption analysis [42,43]. In Fig. 3, it can be seen that if no nanofoams are added to the loading cell, the compression curve is quite rigid, as mercury is nearly incompressible. If a nanofoam is immersed in mercury, initially when the pressure is low, infiltration would not occur, due to the capillary effect. When the critical pressure is exceeded, mercury is forced into the nanopores, causing the formation of an infiltration plateau in the sorption isotherm curve. The largest nanopores are involved in the infiltration process first, and as the pressure increases, smaller nanopores are filled. The relatively flat infiltration plateaus indicate that the pore size distributions of the PPC-treated silica nanofoams are narrow. This is shown more clearly in Fig. 4(b), in which dP/dV fluctuates around zero until almost all the pores are filled. The steep drop at the beginning of the infiltration plateau is associated with the large decrease in effective system compressibility. The width of the infiltration plateau was used to estimate the pore volume of the macropores. As shown in Table 1, the specific pore volume of macropores is about 0.6 cm^3/g, regardless of the pore size; in Table 2, the total specific pore volume is about 0.7 cm^3/g. Thus, about 85% of the pores are on the macroporous level.

Fig. 5 shows the XRD results. The broad peaks around $2\theta \approx 22°$ suggest that the PPC-treated silica nanofoams all exhibit a short range order [44]; that is, the PPC temperature, T_s, in the current investigation does not influence the amorphous nature of the silica

Table 2
The parameters of PPC-treated nanofoams.

Average pore size (nm)	1380	315	240	185	155	120	85	70	50
Diameter (mm)	22.9 ± 0.9	22.6 ± 0.1	22.3 ± 0.3	22.6 ± 0.4	22.6 ± 0.2	23.5 ± 0.3	23.0 ± 0.3	23.7 ± 0.5	24.2 ± 0.3
Thickness (mm)	4.51 ± 0.02	4.51 ± 0.01	4.53 ± 0.01	4.51 ± 0.01	4.53 ± 0.01	4.53 ± 0.01	4.51 ± 0.01	4.52 ± 0.01	4.52 ± 0.01
Porosity (%)	59.6 ± 2.7	62.7 ± 0.9	61.6 ± 0.9	60.7 ± 1.2	59.5 ± 0.8	62.4 ± 1.4	59.1 ± 2.0	60.0 ± 1.5	60.0 ± 1.3
Specific pore volume (cm^3/g)	0.71 ± 0.12	0.76 ± 0.03	0.73 ± 0.03	0.70 ± 0.04	0.67 ± 0.02	0.76 ± 0.05	0.66 ± 0.06	0.68 ± 0.04	0.68 ± 0.04

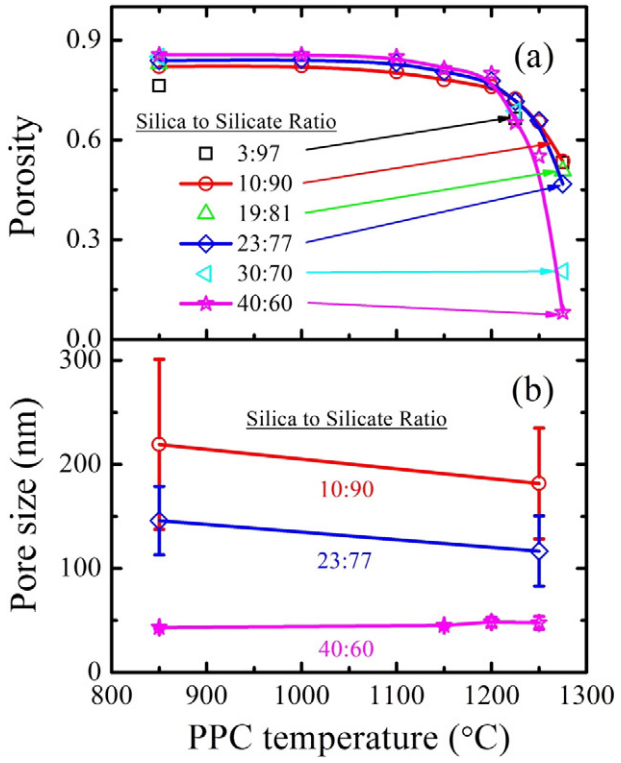

Fig. 2. Effects of the PPC temperature, T_s, on (a) the porosity and (b) the average pore size of silica nanofoams.

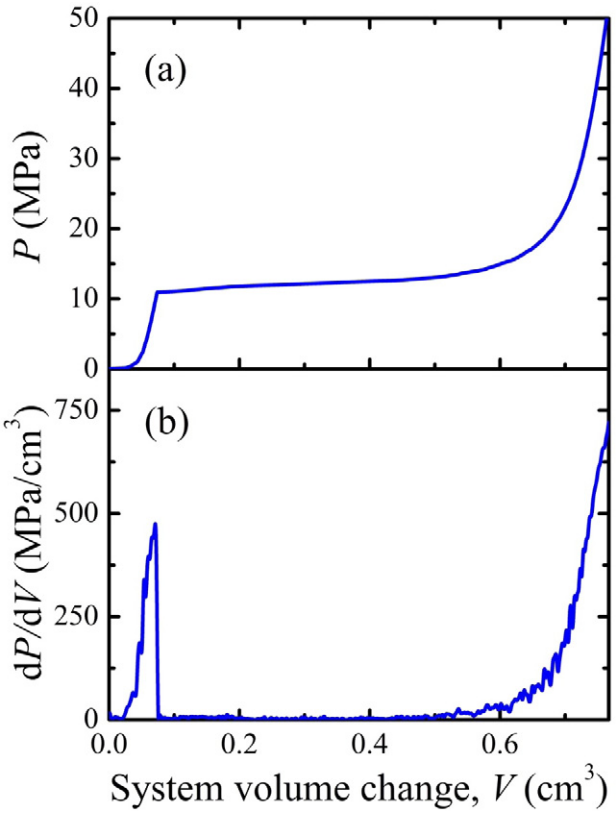

Fig. 4. Definition of the infiltration plateau: (a) a typical sorption isotherm curve showing the relationship between P and V; (b) dP/dV.

phase. Fig. 6 confirms that the porous configurations of PPC-treated silica nanofoams are similar. All the pores are interconnected and open. The ligament length is correlated with the pore size, as it should be.

4. Conclusions

As the calcination temperature varies around the glass transition temperature of amorphous silica, the overall pore size distribution of a silica nanofoam does not change much while the porosity can become significantly different. Based on this phenomenon, a post-processing calcination (PPC) technique is developed to decouple the pore size and the porosity. When the PPC temperatures are appropriately chosen for silica monoliths of different initial pore sizes, their porosities may be adjusted to a similar level while the variations in pore sizes are quite mild. In the current study, the PPC parameters are optimized to obtain silica nanofoams of a similar porosity around 60%, with the pore size broadly ranging from dozens of nm to more than 1 μm.

Acknowledgments

This research was supported by the Army Research Office under Grant No. W911NF-12-1-0011, for which we are grateful to Dr. David M. Stepp.

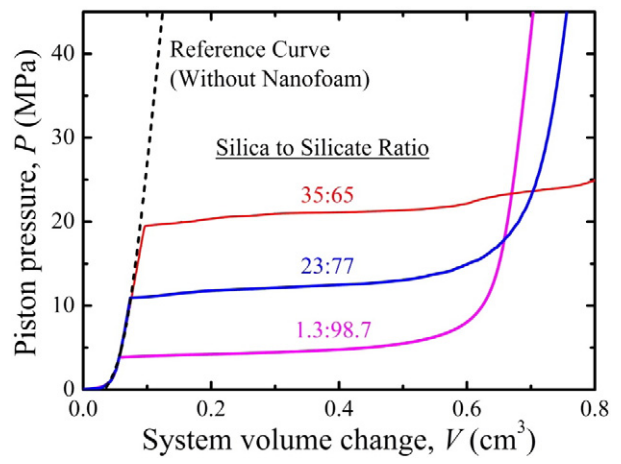

Fig. 3. Typical sorption isotherm curves of mercury porosimetry. The dashed curve is for the reference compression test on mercury, without any nanofoam.

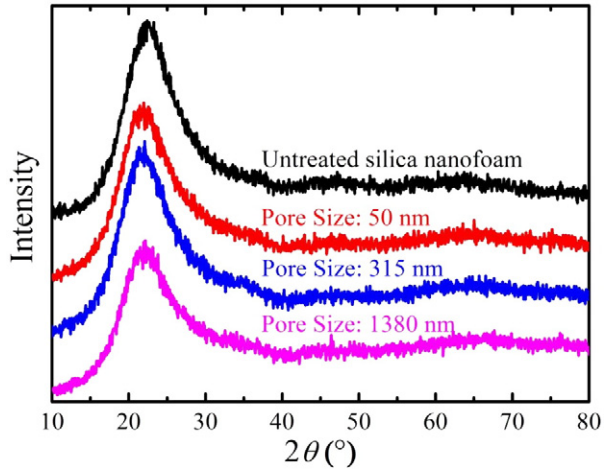

Fig. 5. Typical XRD results. The top curve is for an untreated silica nanofoam, and the bottom three are for PPC-treated nanofoams.

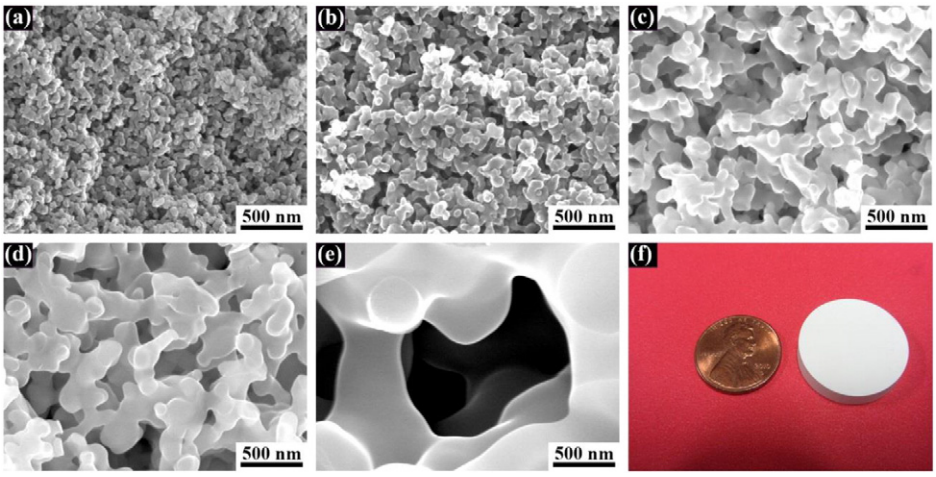

Fig. 6. Typical SEM images of PPC-treated silica nanofoams, with the average pore sizes of (a) 50 nm, (b) 85 nm, (c) 185 nm, (d) 315 nm, and (e) 1380 nm, respectively; (f) photo of a nanofoam sample. The porosities of all the silica nanofoams are ~60%.

References

[1] T. Asefa, C.T. Duncan, K.K. Sharma, Recent advances in nanostructured chemosensors and biosensors, Analyst 134 (2009) 1980–1990.
[2] C.E. Ashley, E.C. Carnes, G.K. Phillips, D. Padilla, P.N. Durfee, P.A. Brown, et al., The targeted delivery of multicomponent cargos to cancer cells by nanoporous particle-supported lipid bilayers, Nat. Mater. 10 (2011) 389–397.
[3] A.M. Md Jani, D. Losic, N.H. Voelcker, Nanoporous anodic aluminium oxide: advances in surface engineering and emerging applications, Prog. Mater. Sci. 58 (2013) 636–704.
[4] G. Schmid, M. Bäumle, M. Geerkens, I. Heim, C. Osemann, T. Sawitowski, Current and future applications of nanoclusters, Chem. Soc. Rev. 28 (1999) 179–185.
[5] A.G. Slater, A.I. Cooper, Function-led design of new porous materials, Science 348 (2015).
[6] T. Titze, C. Chmelik, J. Kullmann, L. Prager, E. Miersemann, R. Gläser, et al., Microimaging of transient concentration profiles of reactant and product molecules during catalytic conversion in nanoporous materials, Angew. Chem. Int. Ed. 54 (2015) 5060–5064.
[7] J.-H. Lee, L. Wang, S. Kooi, M.C. Boyce, E.L. Thomas, Enhanced energy dissipation in periodic epoxy nanoframes, Nano Lett. 10 (2010) 2592–2597.
[8] A. Misra, J.R. Greer, C. Daraio, Strain rate effects in the mechanical response of polymer-anchored carbon nanotube foams, Adv. Mater. 21 (2009) 334–338.
[9] T. Rahman, R. Liu, E. Ortel, R. Kraehnert, A. Antoniou, Mechanical behavior of mesoporous titania thin films, Appl. Phys. Lett. (2014) 104.
[10] J. Zhang, J. Malzbender, Mechanical characterization of micro- and nano-porous alumina, Ceram. Int. 41 (2015) 10725–10729.
[11] J.L. Hedrick, K.R. Carter, J.W. Labadie, R.D. Miller, W. Volksen, C.J. Hawker, et al., H.R. Kricheldorf, Nanoporous polyimides, Progress in Polyimide Chemistry II, Springer Berlin Heidelberg 1999, pp. 1–43.
[12] B.C. Tappan, S.A. Steiner, E.P. Luther, Nanoporous metal foams, Angew. Chem. Int. Ed. 49 (2010) 4544–4565.
[13] K. Nakanishi, Synthesis Concepts and Preparation of Silica Monoliths. Monolithic Silicas in Separation Science: Concepts, Syntheses, Characterization, Modeling and Applications, John Wiley & Sons, 2010 11.
[14] A. Han, Y. Qiao, A volume–memory liquid, Appl. Phys. Lett. 91 (2007) 173123.
[15] S. Ma, H.-C. Zhou, Gas storage in porous metal–organic frameworks for clean energy applications, Chem. Commun. 46 (2010) 44–53.
[16] J.R. Hayes, G. Nyce, J. Kuntz, J. Satcher, A. Hamza, Synthesis of bi-modal nanoporous Cu, CuO and Cu_2O monoliths with tailored porosity, Nanotechnology 18 (2007) 275602.
[17] G.W. Nyce, J.R. Hayes, A.V. Hamza, J.H. Satcher, Synthesis and characterization of hierarchical porous gold materials, Chem. Mater. 19 (2007) 344–346.
[18] I. Vukovic, G. Brinke, K. Loos, Block copolymer template-directed synthesis of well-ordered metallic nanostructures, Polymer 54 (2013) 2591–2605.
[19] F. Svec, J.M. Frechet, Kinetic control of pore formation in macroporous polymers. Formation of "molded" porous materials with high flow characteristics for separations or catalysis, Chem. Mater. 7 (1995) 707–715.
[20] T. Kanazawa, Y. Matsuda, S. Tasaka, Fabrication of a porous structure of poly (tetrafluoroethylene) from a mixture with fumaric acid, Polym. J. (2010).
[21] J. Pinto, M. Dumon, M. Pedros, J. Reglero, M.A. Rodriguez-Perez, Nanocellular CO_2 foaming of PMMA assisted by block copolymer nanostructuration, Chem. Eng. J. 243 (2014) 428–435.
[22] R.D. Shoup, Controlled pore silica bodies gelled from silica sol-alkali silicate mixtures, in: M. Kerker (Ed.), Colloid and Interface Science, Academic Press, New York 1976, pp. 63–69.
[23] I.-K. Sung, S.-B. Yoon, J.-S. Yu, D.-P. Kim, Fabrication of macroporous SiC from templated preceramic polymers, Chem. Commun. 1480-1 (2002).
[24] Y. Tokudome, K. Fujita, K. Nakanishi, K. Miura, K. Hirao, Synthesis of monolithic Al_2O_3 with well-defined macropores and mesostructured skeletons via the sol–gel process accompanied by phase separation, Chem. Mater. 19 (2007) 3393–3398.
[25] C.J. Brinker, G.W. Scherer, Sol–Gel Science: The Physics and Chemistry of Sol–Gel Processing, Gulf Professional Publishing, 1990.
[26] P. Levitz, G. Ehret, S.K. Sinha, J.M. Drake, Porous vycor glass: the microstructure as probed by electron microscopy, direct energy transfer, small-angle scattering, and molecular adsorption, J. Chem. Phys. 95 (1991) 6151–6161.
[27] M. Schmidt, F. Schwertfeger, Applications for silica aerogel products, J. Non-Cryst. Solids 225 (1998) 364–368.
[28] Y. Qiao, G. Cao, X. Chen, Effects of gas molecules on nanofluidic behaviors, J. Am. Chem. Soc. 129 (2007) 2355–2359.
[29] C. Largeot, C. Portet, J. Chmiola, P.-L. Taberna, Y. Gogotsi, P. Simon, Relation between the ion size and pore size for an electric double-layer capacitor, J. Am. Chem. Soc. 130 (2008) 2730–2731.
[30] J. Pinto, M. Dumon, M. Pedros, J. Reglero, M.A. Rodriguez-Perez, Nanocellular CO_2 foaming of PMMA assisted by block copolymer nanostructuration, Chem. Eng. J. 243 (2014) 428–435.
[31] K. Kanamori, J. Hasegawa, K. Nakanishi, T. Hanada, Facile synthesis of macroporous cross-linked methacrylate gels by atom transfer radical polymerization, Macromolecules 41 (2008) 7186–7193.
[32] K. Nakanishi, Pore structure control of silica gels based on phase separation, J. Porous. Mater. 4 (1997) 67–112.
[33] R. Miyamoto, Y. Ando, C. Kurusu, B. Hz, K. Nakanishi, M. Ippommatsu, J. Sep. Sci. 36 (2013) 1890–1896.
[34] T. Kawaguchi, J. Iura, N. Taneda, H. Hishikura, Y. Kokubu, Structural changes of monolithic silica gel during the gel-to-glass transition, J. Non-Cryst. Solids 82 (1986) 50–56.
[35] Y. Diao, T. Harada, A.S. Myerson, T. Alan Hatton, B.L. Trout, The role of nanopore shape in surface-induced crystallization, Nat. Mater. 10 (2011) 867–871.
[36] L.J. Gibson, M.F. Ashby, Cellular Solids: Structure and Properties, Cambridge University Press, 1999.
[37] E.W. Washburn, The dynamics of capillary flow, Phys. Rev. 17 (1921) 273–283.
[38] R. Pirard, C. Alie, J.-P. Pirard, Specific behavior of sol–gel materials in mercury porosimetry: collapse and intrusion, Handbook of Sol–Gel Science and Technology Volume II: Characterization of Sol–Gel materials and Products 2005, pp. 211–233.
[39] J. Frenkel, Viscous flow of crystalline bodies under the action of surface tension, J. Phys. 9 (1945) 385–391.
[40] J. Mackenzie, High-pressure effects on oxide glasses: III, densification in nonrigid state, J. Am. Ceram. Soc. 47 (1964) 76–80.
[41] R.K. Iler, The Chemistry of Silica: Solubility, Polymerization, Colloid and Surface Properties, and Biochemistry, Wiley, 1979.
[42] S. Lowell, Characterization of Porous Solids and Powders: Surface Area, Pore Size and Density, Springer, 2004.
[43] R.P. Mayer, R.A. Stowe, Mercury porosimetry—breakthrough pressure for penetration between packed spheres, J. Colloid Sci. 20 (1965) 893–911.
[44] C. Suryanarayana, M.G. Norton, X-ray Diffraction: A Practical Approach, Springer, 1998.